PHYSICAL REVIEW E VOLUME 54, NUMBER 3 SEPTEMBER 1996

# Classical and quantum chaos in a quantum dot in time-periodic magnetic fields

R. Badrinarayanan and Jorge V. José
*Department of Physics and Center for Interdisciplinary Research on Complex Systems, Northeastern University, Boston, Massachusetts 02115*

(Received 27 June 1995; revised manuscript received 1 April 1996)

We investigate the classical and quantum dynamics of an electron confined to a circular quantum dot in the presence of homogeneous $B_{\mathrm{dc}}+B_{\mathrm{ac}}$ magnetic fields. The classical motion shows a transition to chaotic behavior depending on the ratio $\epsilon=B_{\mathrm{ac}}/B_{\mathrm{dc}}$ of field magnitudes and the cyclotron frequency $\tilde{\omega}_c$ in units of the drive frequency. We determine a phase boundary between regular and chaotic classical behavior in the $\epsilon$ vs $\tilde{\omega}_c$ plane. In the quantum regime we evaluate the quasienergy spectrum of the time-evolution operator. We show that the nearest-neighbor quasienergy eigenvalues show a transition from level clustering to level repulsion as one moves from the regular to chaotic regime in the $(\epsilon,\tilde{\omega}_c)$ plane. The $\Delta_3$ statistic confirms this transition. In the chaotic regime, the eigenfunction statistics coincides with the Porter-Thomas prediction. Finally, we explicitly establish the phase-space correspondence between the classical and quantum solutions via the Husimi phase-space distributions of the model. Possible experimentally feasible conditions to see these effects are discussed. [S1063-651X(96)02809-7]

PACS number(s): 05.45.+b, 03.65.−w

## I. INTRODUCTION

In this paper we present results of a study of the behavior of an electron confined to a disk of finite radius, subjected to spatially uniform, constant ($B_{\mathrm{dc}}$) plus time-varying ($B_{\mathrm{ac}}$) perpendicular magnetic fields. This allows us to analyze an old problem that exhibits some very unexpected behavior because of the time-dependent field. Without this time-varying component of the field, the electronic states form the oscillatorlike Landau levels [1]. With the addition of confinement, this constant field problem was studied in great detail by Dingle [2]. He obtained perturbative solutions and subsequently others obtained numerical and exact [3] solutions. The solutions depend on the ratio of the cyclotron radius $\rho_c$ to the confinement radius $R_0$. One of the most important consequences of confinement is the presence of "skipping orbits," which play an important role, for example, in the quantum Hall effect [4].

This problem is of significant interest as a consequence of two independent developments over the past few years: one, the important advances in our knowledge of classical chaos [5] and, to a lesser extent, its quantum and semiclassical counterparts [6], and two, the spectacular advances in the fabrication of very clean mesoscopic quantum devices [7], where a high-mobility two-dimensional electron gas is trapped within a boundary of controlled shape. We attempt to begin to bring the two fields together by asking how this model system behaves from the classical dynamical point of view and what its quantum signatures are. We predict ranges of fields and frequencies where some different effects may be experimentally observable. In this paper we consider the single-electron case and leave for a future paper the many-electron problem.

This paper is organized as follows. In Sec. II we define the model with its classical and quantum-mechanical properties, elucidate the important parameters in the problem, and describe the general method of solution. In Sec. III we investigate the properties of the classical model. Based on a combination of analytic and numerical analysis, we obtain a "phase diagram" in the parameter space of the system, which separates the quasi-integrable from the chaotic regions. This phase diagram is shown in Fig. 1. The vertical axis is the ratio $\epsilon=B_{\mathrm{ac}}/B_{\mathrm{dc}}$ of the magnitudes of the fields and the horizontal axis is the Larmor frequency normalized to the ac drive frequency $\tilde{\omega}_c=\omega_c/\omega_0$. This phase diagram is of paramount importance in making the connection between the classical and quantum solutions. The values of the dc field $B_{\mathrm{dc}}$ and drive frequency $\omega_0$ depend on the radius of the dot $R_0$ and certain other parameters. However, to give an

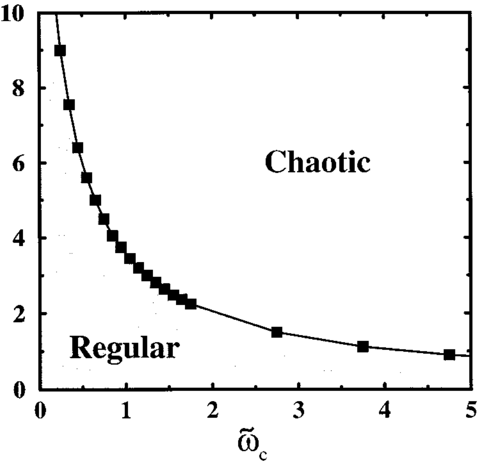

FIG. 1. Classical phase diagram for the problem, obtained from the Lyapunov exponent, calculated as explained in Sec. III. The vertical axis $\epsilon$ is the strength of the ac magnetic field $B_{\mathrm{ac}}$ relative to the dc field $B_{\mathrm{dc}}$, while the horizontal axis $\tilde{\omega}_c$ is the Larmor frequency associated with $B_{\mathrm{dc}}$ relative to the "kick" frequency $\omega_0$. The shape of the phase boundary is fairly insensitive to the value of the threshold Lyapunov exponent $\lambda_c$ chosen to characterize hard chaos (here $\lambda_c=1.0$). The boundary is well fitted by the relation $\epsilon=C(\lambda_c)/\tilde{\omega}_c$, with $C(\lambda_c=1.0)\approx1.0$ (see the text for more details).

© 1996 The American Physical Society

idea of the magnitudes of the physical parameters involved, let us pick two representative points on the diagram: $(\tilde{\omega}_c, \epsilon) = (0.1, 0.1)$ corresponds to $\omega_0 = 20$ GHz and $B_{\mathrm{dc}} = 20$ G when $R_0 = 1$ $\mu$m, while $\omega_0 = 800$ MHz and $B_{\mathrm{dc}} = 0.08$ G for $R_0 = 5$ $\mu$m. Similarly, $(\tilde{\omega}_c, \epsilon) = (2.0, 2.0)$ corresponds to $\omega_0 = 20$ GHz and $B_{\mathrm{dc}} = 800$ G for $R_0 = 1$ $\mu$m, while $\omega_0 = 20$ GHz and $B_{\mathrm{dc}} = 32$ G for $R_0 = 5$ $\mu$m. The details of the these estimates are presented in Sec. V.

We analytically obtain conditions and look at various kinds of fixed points of the classical solutions. In Sec. IV we study the spectral statistics of the quantum evolution operator, which shows clear signatures of the classical transition from quasi-integrability to chaos. We also discuss the eigenfunction properties in different regimes using the $\chi^2$ distribution of $\nu$ freedoms as a convenient parametrization of the results. Then we turn to semiclassical correspondences, where we use a phase-space approach to the quantum eigenfunctions and make direct connections with various types of classical phase-space periodic orbits. In Sec. V we discuss possible experimental scenarios where the predicted effects may be observable. Finally, in Sec. VI we summarize our results and present our conclusions.

## II. MODEL

The model of a quantum dot we consider here is that of an electron confined to a disk of radius $R_0$ subject to steady (dc) and time-periodic (ac) magnetic fields. Choosing the cylindrical gauge, where the vector potential $\mathbf{A}(\vec{\rho},t) = \frac{1}{2}B(t)\rho\hat{\boldsymbol{e}}_\phi$, $B(t)$ being the time-dependent magnetic field, the quantum-mechanical single-particle Hamiltonian in the coordinate representation is given by

$$H = -\frac{\hbar^2}{2m^*}\left(\frac{d^2}{d\rho^2} + \frac{1}{\rho}\frac{d}{d\rho} + \frac{1}{\rho^2}\frac{d^2}{d\phi^2}\right) + \frac{1}{8}m^*\Omega^2(t)\rho^2 + \frac{1}{2}\Omega(t)L_z, \quad 0 \leqslant \rho \leqslant R_0, \tag{1}$$

where $m^*$ is the effective mass of the electron (roughly $0.067m_e$ in GaAs-Al$_x$Ga$_{1-x}$As semiconductor quantum dots) [7], $L_z$ is the operator of the conserved angular momentum, and $\Omega(t) = eB(t)/m^*c$, $e$ and $c$ being the electronic charge and the speed of light, respectively. Let the magnetic field be of the form $B(t) = B_{\mathrm{dc}} + B_{\mathrm{ac}}f(t)$, where $f(t) = f(t+T_0)$ is some periodically time-varying function. We can separate the Hamiltonian $H = H_{\mathrm{dc}} + H_1(t)$, where

$$H_{\mathrm{dc}} = -\frac{\hbar^2}{2m^*}\left(\frac{d^2}{d\rho^2} + \frac{1}{\rho}\frac{d}{d\rho}\right) + \frac{\hbar^2 l^2}{2m^*}\frac{1}{\rho^2} + \frac{1}{8}m^*\omega_c^2(t)\rho^2 + \frac{1}{2}\frac{l\hbar\omega_c}{2}, \tag{2}$$

and $H_1(t) = \frac{1}{8}m^*[2B_{\mathrm{dc}}B_{\mathrm{ac}}f(t) + B_{\mathrm{ac}}^2 f^2(t)]\rho^2$. Here $H_{\mathrm{dc}}$ is the standard static Hamiltonian for a charge in a homogeneous constant perpendicular magnetic field, which includes the para- and diamagnetic contributions, with $\omega_c = eB_{\mathrm{dc}}/m^*c$. With the additional dropping of a term of the form $L_z B_{\mathrm{ac}} f(t)$, which can trivially be removed by a unitary transformation, $H_1(t)$ gives the time-dependent contribution to $H$. Note that $H_1(t) = H_1(t+T_0)$. In the limit in which $H_1(t)$ is much smaller than $H_{\mathrm{dc}}$ one can study the modification to the solutions associated with $H_{\mathrm{dc}}$ by standard time-dependent perturbation theory. As can be seen from the classical phase diagram given in Fig. 1, the boundary between regular and chaotic behavior in fact occurs for $\epsilon = B_{\mathrm{ac}}/B_{\mathrm{dc}} > 1$ and $\tilde{\omega}_c > 1$. We are then led to approximate $H_1(t)$ by

$$H_1(t) = \frac{1}{8}m^*\left((\epsilon\omega_c)^2 \sum_{n=-\infty}^{\infty} \delta(t - nT_0)\right)\rho^2. \tag{3}$$

With this simplification, the Hamiltonian (1) is then approximated by the sum of Eqs. (2) and (3). This choice is also motivated by the following factors. First its calculational ease. The $\delta$ function is the paradigm for time-dependent systems because one can proceed further in the analysis without recourse to drastic approximations. Next are the effects of chaos. Since our primary objective is to explore the quantum manifestations of classical chaos, we are more interested in the general issues of chaos rather than specific functional forms. Even for a more ‘‘physical’’ choice of $f(t) = A\cos(\omega t)$, one can easily show that the resulting functional form of $\Omega^2(t)$ can be approximated sensibly as above. Finally, there are classical considerations. As shown in the Appendix, starting from the Lorenz force plus Maxwell's equations, one can write the classical equations of motion *exactly* including the self-induced fields, even for the magnetic field given by $B(t) = B_{\mathrm{dc}} + B_{\mathrm{ac}} T_0 \Sigma_{n=-\infty}^{\infty} \delta(t - nT_0)$. Classically, the associated Lagrangian is linear in the vector potential. There are regularization problems, however, when using this form in the quantum Hamiltonian, since in this case there is an ill-defined $A_{\mathrm{ac}}^2(t)$ term present. However, the model $H = H_{\mathrm{dc}} + H_1$ is well defined.

In order to more clearly see what the relevant parameters in the problem are, we go over to dimensionless units, defined by rescaling all lengths to the disk radius $R_0$, all masses by the effective mass $m^*$, and all times by the period of the ac field $T_0$. Thus we define

$$r = \rho/R_0, \quad 0 \leqslant r \leqslant 1 \tag{4a}$$

$$\tau = t/T_0 \equiv \frac{\omega_0}{2\pi}t, \quad \tilde{\omega}_c = \omega_c/\omega_0, \quad \tilde{\hbar} = \frac{\hbar}{m^*\omega_0 R_0^2}. \tag{4b}$$

In these units, Eqs. (2) and (3) become

$$\tilde{H} = \tilde{H}_{\mathrm{dc}} + \tilde{H}_1(\tau), \tag{5a}$$

$$\tilde{H}_{\mathrm{dc}} = -\frac{\tilde{\hbar}^2}{2}\left(\frac{d^2}{dr^2} + \frac{1}{r}\frac{d}{dr}\right) + \frac{l^2\tilde{\hbar}^2}{2r^2} + \frac{1}{2}\left(\frac{\tilde{\omega}_c}{2}\right)^2 r^2 + l\tilde{\hbar}\frac{\tilde{\omega}_c}{2}, \tag{5b}$$

$$\tilde{H}_1(\tau) = \frac{1}{2}\eta r^2 \sum_{n=-\infty}^{\infty} \delta(\tau - n), \tag{5c}$$

where

$$\eta = \left(\frac{\epsilon\tilde{\omega}_c}{2}\right)^2 \tag{5d}$$

and the corresponding solutions to the time-independent part, along with the boundary and normalization conditions, are given by

$$\tilde{H}_{\mathrm{dc}}\tilde{\Psi}_{nl}(r,\phi)=\tilde{E}_{nl}\tilde{\psi}_{nl}(r)\frac{e^{il\phi}}{\sqrt{2\pi}}, \tag{6a}$$

$$\tilde{\Psi}(r,\phi)=\sum_{n=1}^{\infty}\sum_{l=-\infty}^{\infty}\tilde{\psi}_{nl}(r)\frac{e^{il\phi}}{\sqrt{2\pi}}, \tag{6b}$$

$$\tilde{\psi}_{nl}(r=1)=0, \qquad \int_0^1\tilde{\psi}_{nl}^2(r)r\,dr=1. \tag{6c}$$

As pointed out by Dingle [2], the physically acceptable solutions to Eqs. (6) are the Whittaker functions of the first kind [8]

$$\tilde{\psi}_{nl}(r)=\sqrt{\frac{2}{N_{nl}}\frac{1}{r}}\,M_{\chi_{nl},|l|/2}(2\pi Fr^2), \tag{7}$$

where the frustration parameter $F=\Phi/\Phi_0$ is the ratio of the flux threading the dot to the quantum of flux $\Phi_0=h/2e$. The quantities $\chi_{nl}$ are related to the eigenvalues via

$$\chi_{nl}=\tfrac{1}{2}(\tilde{E}_{nl}-l) \tag{8}$$

and are determined precisely by the requirement that the wave function vanishes at the boundary [Eq. (6c)] $M_{\chi_{nl},|l|/2}(F)=0$. In the limit of no confinement $R_0\to\infty$, we recover the usual Laguerre polynomial solutions for the $\tilde{\psi}_{nl}$'s.

The frustration parameter $F$ can also be written as

$$F=\frac{1}{4\pi}\left(\frac{R_0}{l_H}\right)^2 \quad \text{where} \quad l_H=\left(\frac{\hbar c}{eB_{\mathrm{dc}}}\right)^{1/2}, \tag{9}$$

that is, it is proportional to the square of the ratio of the confinement radius to the magnetic length. When $2\pi F\ll 1$, the problem is equivalent to that of a nearly free electron, bound by a very weak magnetic field, and so is amenable to a perturbative treatment. In the opposite limit, the boundary can essentially be neglected and we recover the results of Dingle mentioned previously. It is in the intermediate regime, when the two lengths are comparable, that we expect the effects of confinement to be nontrivial, especially in the presence of strong time-dependent fields.

In principle, we are able to cover the entire range of parameter values within the same framework by means of a numerical evaluation of the Whittaker functions. However, the Whittaker functions are not very well suited to large-scale computations because of the time required to evaluate each individual function. We choose instead to perform most of our calculations in a Fourier sine basis, which is numerically much faster, and use the Whittaker basis as a check on our results. Choosing the (orthonormalized) basis functions as

$$\chi_{nl}=\sqrt{\frac{2}{r}}\sin(n\pi r)\frac{e^{il\phi}}{\sqrt{2\pi}}, \tag{10}$$

one can show, after a straightforward calculation, that the matrix elements of $\tilde{H}_{\mathrm{dc}}$ are given by

$$\begin{aligned}(\tilde{H}_{\mathrm{dc}})_{mn}=&\left\{\frac{\tilde{\hbar}^2}{2}(n\pi)^2+n\pi(l^2-\tfrac{1}{4})\tilde{\hbar}^2\mathrm{Si}(2n\pi)\right.\\&\left.+\frac{1}{2}\left(\frac{\tilde{\omega}_c}{2}\right)^2\left(\frac{1}{3}-\frac{1}{2n^2\pi^2}\right)+l\tilde{\hbar}\frac{\tilde{\omega}_c}{2}\right\}\delta_{mn}\\&+\left\{\frac{\pi}{2}(l^2-\tfrac{1}{4})\tilde{\hbar}^2\{(m+n)\mathrm{Si}[(m+n)\pi]\right.\\&-(m-n)\mathrm{Si}[(m-n)\pi]\}\\&\left.+\frac{1}{2}\left(\frac{\tilde{\omega}_c}{2}\right)^2\frac{(-1)^{m+n}}{\pi^2}\frac{8mn}{(m^2-n^2)^2}\right\}(1-\delta_{mn}),\end{aligned} \tag{11}$$

where $\mathrm{Si}(x)$ is the Sine integral. One can similarly compute matrix elements of other needed operators.

Having worked out a suitable set of basis functions, we now proceed to tackle the full time-dependent problem. The Schrödinger equation for the time evolution operator is

$$i\tilde{\hbar}\frac{\partial}{\partial\tau}U(\tau,\tau_0)=[\tilde{H}_{\mathrm{dc}}+\tilde{H}_1(\tau)]U(\tau,\tau_0). \tag{12}$$

Since we have a periodic system $\tilde{H}(\tau+1)=\tilde{H}(\tau)$ from the Floquet theorem [9], it is sufficient to determine the one-period time evolution operator $U(\tau_0+1,\tau_0)$ from

$$i\tilde{\hbar}\frac{\partial}{\partial\tau}U(\tau)=[\tilde{H}_{\mathrm{dc}}+\tilde{V}_1(\tau)]U(\tau), \quad 0<\tau\leqslant 1 \tag{13a}$$

$$\tilde{V}_1(\tau)=\tilde{V}\delta(\tau-1) \quad \text{where} \quad \tilde{V}=\frac{1}{2}\eta r^2, \tag{13b}$$

where the parameter $\eta$ has been defined previously. All the information about the dynamics of the system is contained within this Floquet operator since $\Phi(r,\phi,\tau+1)=U\Phi(r,\phi,\tau)$, where $\Phi$ is the total wave function. Because of the periodic $\delta$-kicked dynamics, we can immediately integrate Eq. (13a) to get

$$U_l(1,0)=\exp\left(-\frac{i}{\tilde{\hbar}}\tilde{V}\right)\exp\left(-\frac{i}{\tilde{\hbar}}\tilde{H}_{\mathrm{dc}}\right). \tag{14}$$

The subscript $l$ has been attached to $U$ to emphasize that the evolution operator has been restricted to that single $l$ value. In other words, states with different values of $l$ evolve independently, an immediate consequence of the conservation of angular momentum in this system. The rightmost exponential operator in Eq. (14) evolves the wave function from just after the ''kick'' at $\tau=0$ to just before the kick at one period under the influence of $\tilde{H}_{\mathrm{dc}}$, while the operator to its left propagates it from just before to just after the kick at a period.

Since $U$ is a unitary operator, the spectrum of its eigenvalues can be represented as

$$U_l \phi_{nl} = e^{i\varepsilon_{nl}} \phi_{nl} . \tag{15}$$

The set of eigenvalues $\{\varepsilon_{nl} \in (0,2\pi)\}$ is collectively known as the quasienergy eigenvalues (QEE's) and the eigenfunctions $\{\phi_{nl}\}$ as the quasienergy eigenfunctions (QEF's) of $U$. The investigation of the quantum dynamics of the system is completely equivalent to determining the nature of the QEE's and QEF's. The fundamental task is thus to obtain the quasienergy spectrum of the evolution operator given by Eq. (14).

## III. CLASSICAL DYNAMICS

We begin the discussion of the behavior of the model by looking at its classical dynamics. The classical Hamiltonian corresponding to the quantum one given by Eqs. (5) is

$$\widetilde{H} = \widetilde{H}_{\rm dc} + \widetilde{H}_1(\tau), \tag{16a}$$

$$\widetilde{H}_{\rm dc} = \tfrac{1}{2} p_r^2 + \frac{J^2}{2r^2} + \frac{1}{2}\left(\frac{\widetilde{\omega}_c}{2}\right)^2 r^2 + J\frac{\widetilde{\omega}_c}{2}, \tag{16b}$$

$$\widetilde{H}_1(\tau) = \tfrac{1}{2}\, \eta r^2 \sum_{n=-\infty}^{\infty} \delta(\tau - n), \tag{16c}$$

where $p_r$ is the radial momentum and $J$ is the *conserved* angular momentum. To make quantitative correspondences between the classical and quantum results, we always set the numerical values of the angular momenta in the two cases to be equal, i.e., we set $J = l\widetilde{\hbar}$.

In between the kicks at a period, and as long as it does not hit the boundary at $r=1$, the electron's motion is governed by the static Hamiltonian $\widetilde{H}_{\rm dc}$. The equation of motion in this case is

$$\ddot{r} = -\left(\frac{\widetilde{\omega}_c}{2}\right)^2 r + \frac{J^2}{r^3}, \tag{17}$$

whose solution, in terms of the energy $E$,

$$E = \tfrac{1}{2} p_r^2 + \frac{J^2}{2r^2} + \frac{1}{2}\left(\frac{\widetilde{\omega}_c}{2}\right)^2 r^2 + J\frac{\widetilde{\omega}_c}{2}, \tag{18}$$

is given by

$$\begin{pmatrix} r(\tau) \\ p_r(\tau) \end{pmatrix} = \begin{pmatrix} \sqrt{\dfrac{2}{\widetilde{\omega}_c}\left[ b + a \sin\left\{ \widetilde{\omega}_c(\tau - \tau_0) + \sin^{-1}\left( \dfrac{\frac{1}{2}\,\widetilde{\omega}_c r_0^2 - b}{a} \right) \right\} \right]} \\ \dfrac{a}{r(\tau)} \cos\left\{ \widetilde{\omega}_c(\tau - \tau_0) + \sin^{-1}\left( \dfrac{\frac{1}{2}\,\widetilde{\omega}_c r_0^2 - b}{a} \right) \right\} \end{pmatrix}, \tag{19}$$

where

$$b = 2E/\widetilde{\omega}_c - J, \quad a = \sqrt{b^2 - J^2}. \tag{20}$$

Here $r_0$ and $\tau_0$ are initial conditions. For a given energy $E$, the motion is constrained by the centrifugal barrier on one side and the smaller of the wall radius (equal to 1) and the constraint imposed by the attractive quadratic potential on the other:

$$r_{\rm min} \leqslant r(\tau) \leqslant \min\{r_{\rm max}, 1\}, \tag{21a}$$

where

$$r_{\rm min} = \sqrt{\frac{2}{\widetilde{\omega}_c}(b-a)}, \quad r_{\rm max} = \sqrt{\frac{2}{\widetilde{\omega}_c}(b+a)}. \tag{21b}$$

Note that the equations of motion are nonlinear here, even in the wall's absence. The effect of collision with the wall (or centrifugal barrier) is simply to reverse the direction of motion

$$\begin{pmatrix} r(\tau_c^+) \\ p_r(\tau_c^+) \end{pmatrix} = \begin{pmatrix} 1 & 0 \\ 0 & -1 \end{pmatrix} \begin{pmatrix} r(\tau_c^-) \\ p_r(\tau_c^-) \end{pmatrix}, \tag{22}$$

where $\tau_c$ is the time of collision with the wall (or barrier). Finally, the effects of the kicks at $\tau = n$ are obtained by integrating the equations of motion over an infinitesimal duration around $n$:

$$\begin{pmatrix} r(n^+) \\ p_r(n^+) \end{pmatrix} = \begin{pmatrix} 1 & 0 \\ \eta r & 1 \end{pmatrix} \begin{pmatrix} r(n^-) \\ p_r(n^-) \end{pmatrix}. \tag{23}$$

If we denote the mapping due to the "free" evolution of the particle under the influence of $H_{\rm dc}$ by $M_0$ [Eqs. (19)], that due to the walls by $M_{\rm wall}$ [Eqs. (22)], and the mapping due to the kick by $M_{\rm kick}$ [Eqs. (23)], then the complete one-period map is typically given by the product of several $M$'s for a given energy, i.e.,

$$M_T = (M_0 M_{\rm wall})^N M_{\rm kick} . \tag{24}$$

In general, the map is very complicated and very sensitive to initial conditions. By recording the values at each successive period, we obtain a surface of section of the trajectory of the particle in phase space.

There are three independent parameters in the problem: $\widetilde{\omega}_c$, $\epsilon$, and $\widetilde{\hbar}$. However, for quantitative correspondences to be made later with the quantum results, as mentioned earlier, we keep the angular momentum $J = l\widetilde{\hbar}$ fixed, which reduces

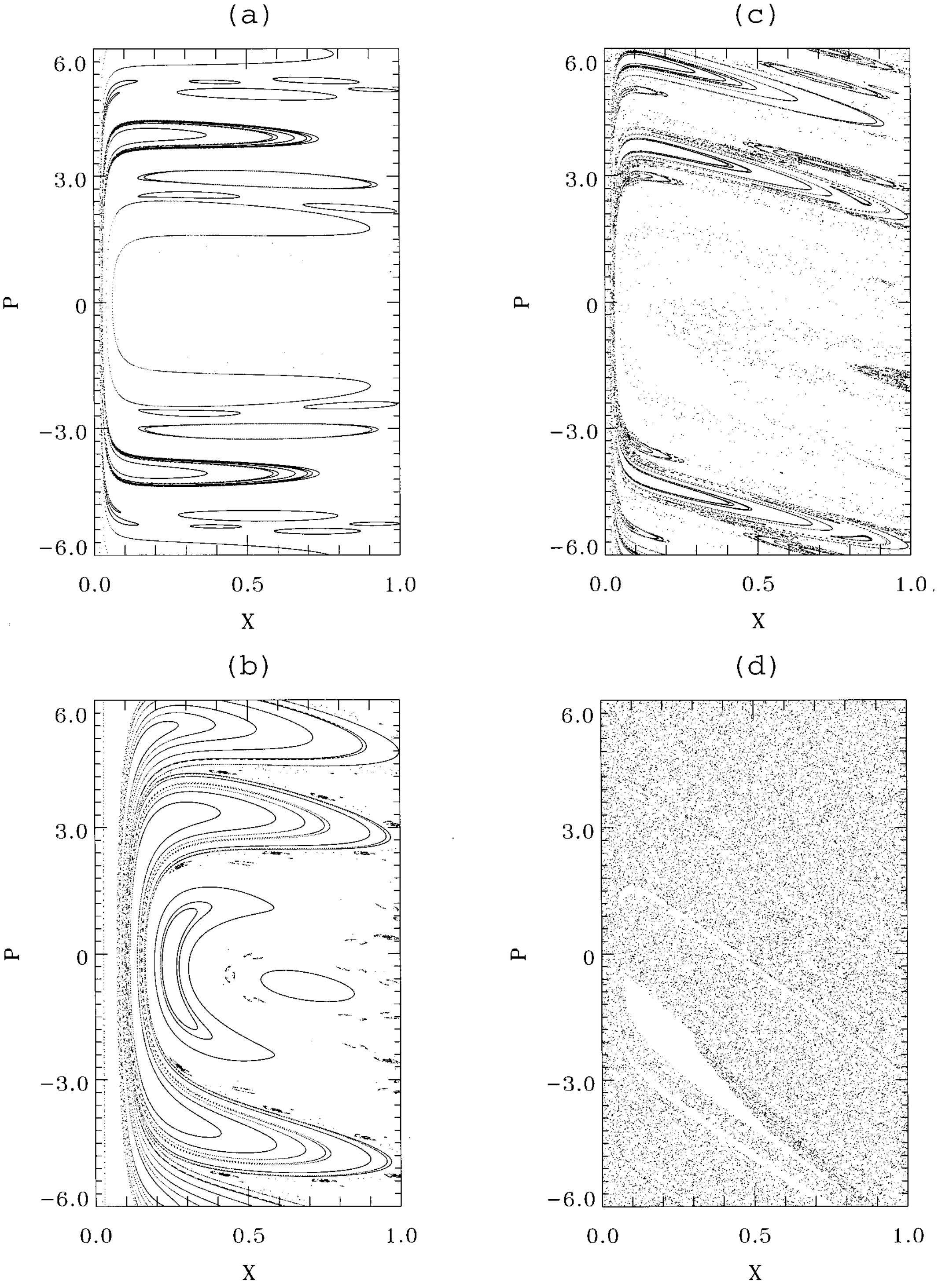

FIG. 2. Poincaré surfaces of section in the $(r,p_r)$ plane. The values of $\epsilon$ are (a) 0.5, (b) 1.5, (c) 1.95, and (d) 2.5. $\tilde{\hbar}=0.01$, $l=10$, and $\tilde{\omega}_c=2.0$ are held fixed. We observe a gradual breakup of the invariant tori while going from (a) to (d) so that eventually there is no longer any structure present in the phase space.

the number of parameters to the first two. The transition to chaos is manifested in the parameter space spanned by $(\epsilon,\tilde{\omega}_c)$ (see Fig. 1). All of our subsequent results refer to this space. We did investigate the effects of varying $J$ by varying $\tilde{\hbar}$ for fixed $l$ and the results are quantitatively very similar.

The first (and most obvious) evidence of chaotic behavior is seen in the Poincaré surface of section in $(r,p_r)$. In Figs. 2(a)–2(d) we show the sections corresponding to $\epsilon$ values of 0.5, 1.5, 1.95, and 2.5, respectively, while $\tilde{\hbar}=0.01$, $\tilde{\omega}_c=2.0$, and $l=5$ are held fixed. [The reason for this particular choice has to do with the $(\epsilon,\tilde{\omega}_c)$ phase diagram for this system, which is explained in more detail shortly.] In the quasi-integrable regime [Figs. 2(a) and 2(b)], the phase space is dominated by invariant tori, which are close to those of the unperturbed problem. As the value of $\tilde{\omega}_c$ is increased, the tori begin to break up and isolated chaotic islands begin to appear [Fig. 2(c)] until, finally, all evidence of invariant curves disappears and all we see is the uniform chaotic sea [Fig. 2(d)]. These values of $(\epsilon,\tilde{\omega}_c)$ corresponding to the integrable, intermediate, and chaotic regions will be retained throughout what follows to make comparisons between the classical and quantum results.

Corresponding to the transition from regular to chaotic behavior, we begin to see the appearance of diffusive growth in the averaged energy (or squared momentum) of a localized ensemble of initial conditions. Figure 3(a) shows the average energy as a function of time for the parameters corresponding to the quasi-integrable regime, while Fig. 3(b) corresponds to parameter values in the chaotic regime. In contrast to the behavior in the quasi-integrable regime, where the energy $E$ is regular, oscillatory quasiperiodic functioning of time around a constant value, in the chaotic regime $E$ grows linearly (or $p_r$ grows quadratically) with time. (Here and subsequently, ''time'' refers to stroboscopic time, just after every kick.)

A quantitative measure of the degree of chaos in the system is to calculate the largest Lyapunov exponent. (In our reduced two-dimensional phase space, since the flow is Hamiltonian, the Lyapunov exponents come in pairs of opposite sign.) Because our phase space is bounded, we use an approach slightly modified from that used for an unbounded system to the calculation of the exponent, as outlined by Reichl [10]. The (largest) Lyapunov exponent is defined by

$$\lambda_n(\tau, \mathbf{X}_{0,0}, \mathbf{Y}_{0,0}) = \frac{1}{n\tau}\sum_{j=1}^{n} \ln\left(\frac{d_j}{d_0}\right), \tag{25}$$

where $d_0 = |\mathbf{Y}_{0,0} - \mathbf{X}_{0,0}|$ is the Euclidean distance between the position of neighboring trajectories labeled by $\mathbf{X}_{0,0}$ and $\mathbf{Y}_{0,0}$, and $\{d_j\}, j=1,\ldots,n$, is the sequence of distances generated between the trajectories at $n$ successive time steps. If $d_0$ is not too large, then the limit $\lim_{n\uparrow\infty}\lambda_n(\tau, \mathbf{X}_{0,0}, \mathbf{Y}_{0,0}) = \lambda(\mathbf{X}_{0,0})$ exists and is independent of both $d_0$ and $\tau$. Furthermore, $\lambda(\mathbf{X}_{0,0})$ is zero if $\mathbf{X}_{0,0}$ is chosen in a regular region, while it is positive if $\mathbf{X}_{0,0}$ is chosen to lie in a chaotic region.

With the help of the Lyapunov exponent we constructed the phase diagram shown in Fig. 1 for this system in the $(\epsilon,\tilde{\omega}_c)$ parameter space in the following fashion. For a given set of parameters $(\epsilon,\tilde{\omega}_c)$, we choose a very large number (typically $10^6$) of initial conditions $\mathbf{X}_{0,0}$ spread uniformly in $(r,p_r)$ phase space. Next we randomly choose a nearby phase-space point $\mathbf{Y}_{0,0}$ within a circle of radius $d_0$, centered about $\mathbf{X}_{0,0}$. We calculate the Lyapunov exponent, using formula (25), from the successive evaluation of the distances $d_j$ for each $j$ iteration of the mapping. This process is repeated for several nearby $\mathbf{Y}_{0,0}$ trajectories. When the Lyapunov exponent reaches saturation we average the resulting value over the set of initial conditions to find $\lambda$. If this asymptotic value is positive, the system is defined as chaotic. To put a stricter criterion on the degree of chaos, we choose a threshold value of the exponent $\lambda_c$ beyond which the system is in the regime of hard chaos. We set $\lambda_c$ arbitrarily equal to the value 1, but as a check we generated Poincaré phase portraits to confirm chaos by looking for featureless (i.e., no invariant tori) phase portraits. In this way, by varying the parameters $(\epsilon,\tilde{\omega}_c)$ in a continuous fashion over the whole plane, running the map repeatedly and obtaining the resulting $\lambda$'s, we obtained the phase diagram for this system, including a distinct ''phase boundary'' separating the quasi-integrable and hard chaos regions. Of course, this phase boundary depends on the precise value of the cutoff $\lambda_c$ we

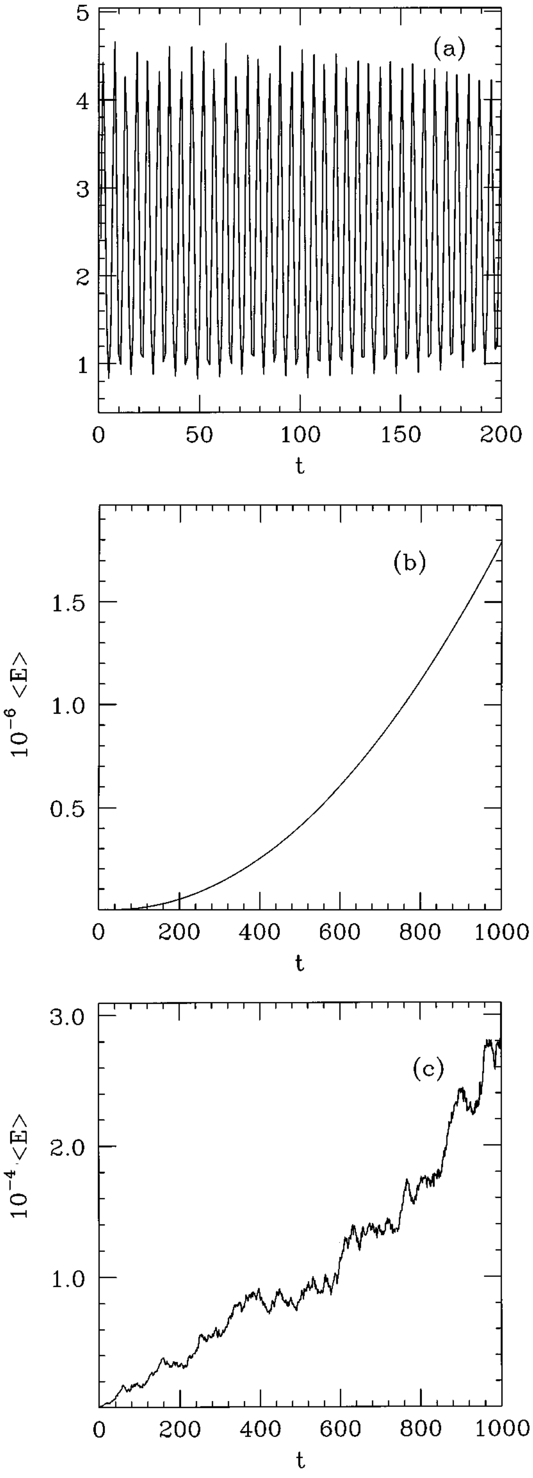

FIG. 3. Average energy of an ensemble of points as a function of time. (a) $\epsilon=0.5$, (b) $\epsilon=1.0$, and (c) $\epsilon=2.5$; all other parameters are as given above. The first is stable and oscillatory, the second shows a quadratic growth in time (see the text), while the third exhibits quasilinear (diffusive) growth, corresponding to particles diffusing through the chaotic sea.

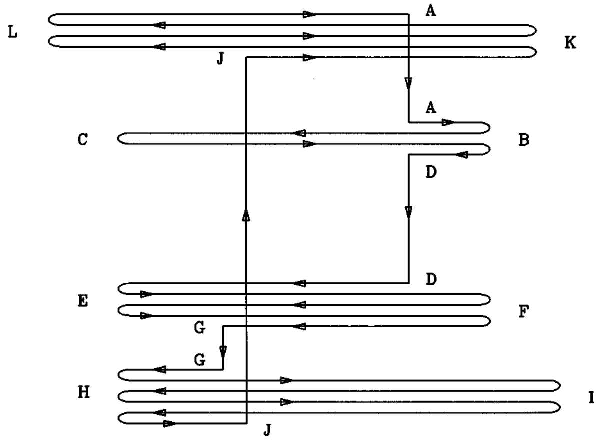

FIG. 4. Schematic trajectory of a period-4 orbit, corresponding to $(\epsilon,\tilde{\omega}_c)=(1.0,2.8284\ldots)$, which is close to the chaos border in Fig. 1.

choose. Nevertheless, we checked that on varying the cutoff $\lambda_c$, the phase boundary shifts only slightly and, furthermore, the shape of the boundary remains qualitatively the same. Indeed, to a high degree of precision, the phase boundary can be fitted by

$$\tilde{\omega}_c = C(\lambda_c)/\epsilon, \tag{26}$$

where $C(\lambda_c)$ is a constant that depends on the value of the cutoff. Figure 1 shows the phase diagram for a cutoff $\lambda_c=1$.

We observe from the classical Poincaré sections that there is a symmetry line in the $(r,p_r)$ plane. This arises from the time-reversal invariance present in the problem as follows. Consider a particle kicked at $\tau=0$. The position $r_0$ remains unchanged, while the momentum changes: $p_r^{(+)}=p_r^{(-)}+\eta r_0$. Denoting $p_r^+$ by $p_0$, then at time $0^{(-)}$ the particle has momentum $p_r^{(-)}=p_0-\eta r_0$. Taking into account the fact that the angular momentum is conserved, we see that propagating a particle *forward* in time from $(r_0,p_0)$ is the same as propagating it *backward* from $(r_0,\eta r_0-p_0)$. Thus the motion is symmetric about the line $p_r=-\frac{1}{2}\eta r$. This symmetry is, of course, present in the quantum problem also, where it will be exploited when calculating the Husimi distributions of the QEF's. In the classical case, we exploit its existence to plot the stable manifolds around hyperbolic fixed points, which are otherwise very difficult to do because of their extreme sensitivity to perturbations.

Although the map is very complicated, there are a few periodic orbit cases that one can analytically study. By following the trajectory of the periodic orbit in phase space, and given the mapping equations, we can reconstruct the initial conditions giving rise to the orbit. For example, the fixed point shown in the Fig. 4 (for $l=5$, $\tilde{\hbar}=0.008$, $\tilde{\omega}_c=2\sqrt{2}$, and $\epsilon=1.0$), labeled $F$, is given by $r_0=0.755\,280\,031\,542\,06\ldots$, $p_0=2.438\,385\,340\,120\,17\ldots$.

## IV. QUANTUM TO CLASSICAL CORRESPONDENCE

As mentioned in the Introduction, one of the clear quantum manifestations of classical chaos emerges when one compares the spectral properties of specific model systems as appropriate parameters are tuned to classically produce a transition from integrable to completely chaotic regimes. In this section we follow the general thinking developed in random matrix theory (RMT) to implement different tests to quantify the spectral properties of the model. These properties are obtained from a direct diagonalization of the one-period time evolution matrix. For the results presented here we vary the value of $\epsilon$ while keeping $J$, $\tilde{\hbar}$, and $\tilde{\omega}_c$ fixed, so as to go from the integrable to the chaotic regime in the phase diagram that coincide with the values considered in the classical case. We note that the appropriate RMT statistical ensemble is a circular orthogonal ensemble rather than a circular unitary ensemble because this model has a false-$T$ breaking symmetry.

Next we discuss the RMT tests and their application to the results obtained for the QEE of our quantum dot model.

### A. Nearest-neighbor QEE distributions

A local measure often used in RMT is the distribution of nearest-neighbor energy level separations $P(s)$, where $s=\varepsilon_{n+1}-\varepsilon_n$. In the extreme integrable and chaotic regimes it has been established [11,12] that $P(s)$ takes the Poisson or Wigner distribution forms

$$P_P(s)=e^{-s}, \quad P_W(s)=\frac{\pi}{2}se^{-(\pi/4)s^2}, \tag{27}$$

respectively. A convenient and often successful parametrization of the $P(s)$ obtained in the transition between $P_P$ to $P_W$ is provided by the Brody interpolation formula [13]

$$P_\nu(s)=\gamma(\nu+1)s^\nu\exp(-\gamma s^{\nu+1}), \tag{28}$$

where $\gamma=[\Gamma((\nu+2)/(\nu+1))]^{\nu+1}$ and $\Gamma(x)$ is the Gamma function. This distribution is normalized and, by construction, has mean spacing $\langle s\rangle=1$. We recover the Poisson case taking $\nu=0$ and Wigner for $\nu=1$. A criticism to the Brody distribution, however, is that there is no first-principles justification for its validity. The fact remains that it does fit the specific results found when considering explicit model systems. Results of the transition, as parametrized by $\nu$, are shown in Fig. 5.

We also calculated higher-order eigenvalue spectral correlations [14]. The average number of levels in an interval of length $L$ is $\langle n(L)\rangle=(1/L\Sigma)_\alpha < n(\alpha,L)$, where the $\langle\ \rangle$ stands for spectral average and $n(\alpha,L)$ is the number of levels in an interval of length $L$ starting at $\alpha$ and ending at $\alpha+L$. Also important are the various moments of the level distribution. The one considered here is the second moment of the average number of levels in a given stretch of length $L$ of the spectrum, the $\Sigma^2(L)$ statistic

$$\langle\Sigma^2(L)\rangle=\langle[n(\alpha,L)-\langle n(\alpha,L)\rangle]^2\rangle. \tag{29}$$

Another often calculated statistic is the Dyson-Mehta $\Delta_3(L)$, which measures the stiffness of the spectrum. This is defined by

$$\Delta_3(L,\alpha)=\frac{1}{L}\min_{A,B}\int_\alpha^{\alpha+L}[\tilde{N}(x)-Ax-B]^2dx, \tag{30}$$

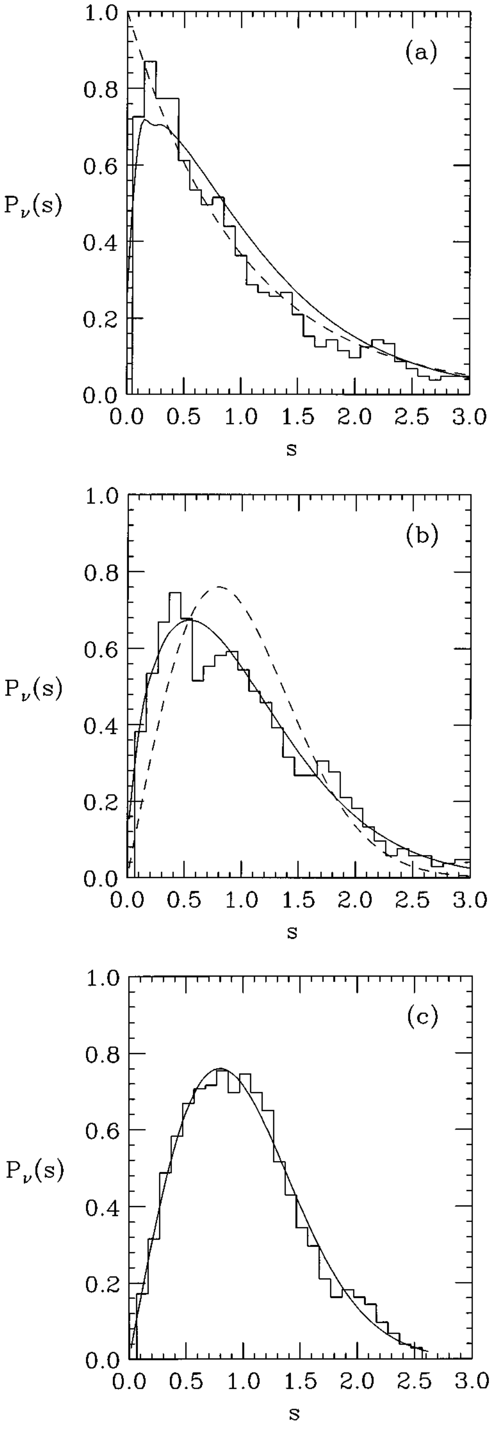

FIG. 5. Nearest-neighbor spacing statistic $P(s)$. Note the gradual movement away from the Poisson to the COE distribution, characterized by the Brody parameters $\nu$ given by (a) 0.27, (b) 0.52, and (c) 1.0, for the $(\epsilon,\tilde{\omega}_c)$ values of Figs. 2(a), 2(c), and 2(d), respectively.

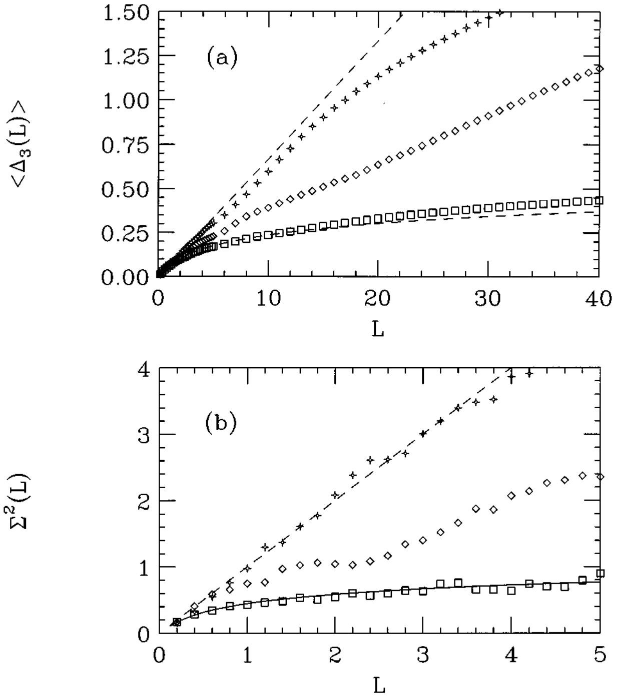

FIG. 6. (a) $\langle\Delta_3(L)\rangle$ and (b) $\Sigma^2(L)$ statistics for the same $(\epsilon,\tilde{\omega}_c)$ values as in Figs. 2(a), 2(c), and 2(d). Again, as $\epsilon$ increases, we observe a transition from Poisson-like (dashed line) to COE-like (solid line) behavior, reflecting the transition to chaos in the classical system.

where $\tilde{N}(x)$ is the unfolded number density. In our case there is no need to unfold the spectrum since it is fully contained between 0 and $2\pi$; $\Delta_3$ is just the least mean-square deviation of $\tilde{N}(x)$ from the mean straight-line behavior. This statistic is directly proportional to the $\langle\Sigma^2\rangle$ by $\Delta_3(L)=(2/L^4)\int_0^L(L^3-sL^2x+x^3)\Sigma^2(x)dx$ and thus can be calculated for the circular orthogonal ensemble (COE) as well [15]. The specific theoretical predictions for the averaged $\langle\Delta_3(L)\rangle=(1/L\Sigma)_\alpha\Delta_3(L,\alpha)$ are $\Delta_3^{(\mathrm{COE})}(L)=(1/\pi^2)\ln\{L\}-0.007$ and $\langle\Delta_3^{(\mathrm{Poisson})}(L)\rangle=L/15$. These results are correct in the asymptotic limit valid for $15\leq L$.

In Fig. 6 we present our results for $\langle\Delta_3\rangle$ and $\langle\Sigma^2\rangle$. In these figures one clearly sees the transition from Poisson-like (dashes) to COE-like (solid line) behavior as $\epsilon/\tilde{\hbar}$ is varied. We note that the $\Delta_3$ statistic does not saturate in the COE limit, even for the maximum interval $L$ that we looked at, as would be expected from semiclassical arguments originally proposed by Berry [16]. Furthermore, note that for the largest $L$ considered the Poisson limit does not present the knee seen in other completely integrable systems as was found before [12]. Generally, the results shown in Fig. 6 are consistent with what we have come to expect for the transition between regular and chaotic regions.

### B. Quasienergy eigenfunction statistics

Here we consider the statistical properties of the eigenfunction overlaps with the natural basis vectors. It has been conjectured [17] that as the classical motion changes from chaotic to regular, this distribution of overlaps can be represented by a $\chi^2$ distribution in $\nu$ degrees of freedom, with $\nu$ varying from 1 in the chaotic regime (the Porter-Thomas limit) to 0 in the regular region (the Poisson limit):

$$P_\nu(y)=\frac{(\nu/2)^{\nu/2}}{\Gamma(\nu/2)}y^{\nu/2-1}\exp(-\nu y/2). \qquad (31)$$

Here $y\equiv|\langle\lambda|nl\rangle|^2$, where $|\lambda\rangle$ labels the QEF and $|nl\rangle$ labels a set of $N$ orthogonal basis vectors. (The $y$'s have been re-

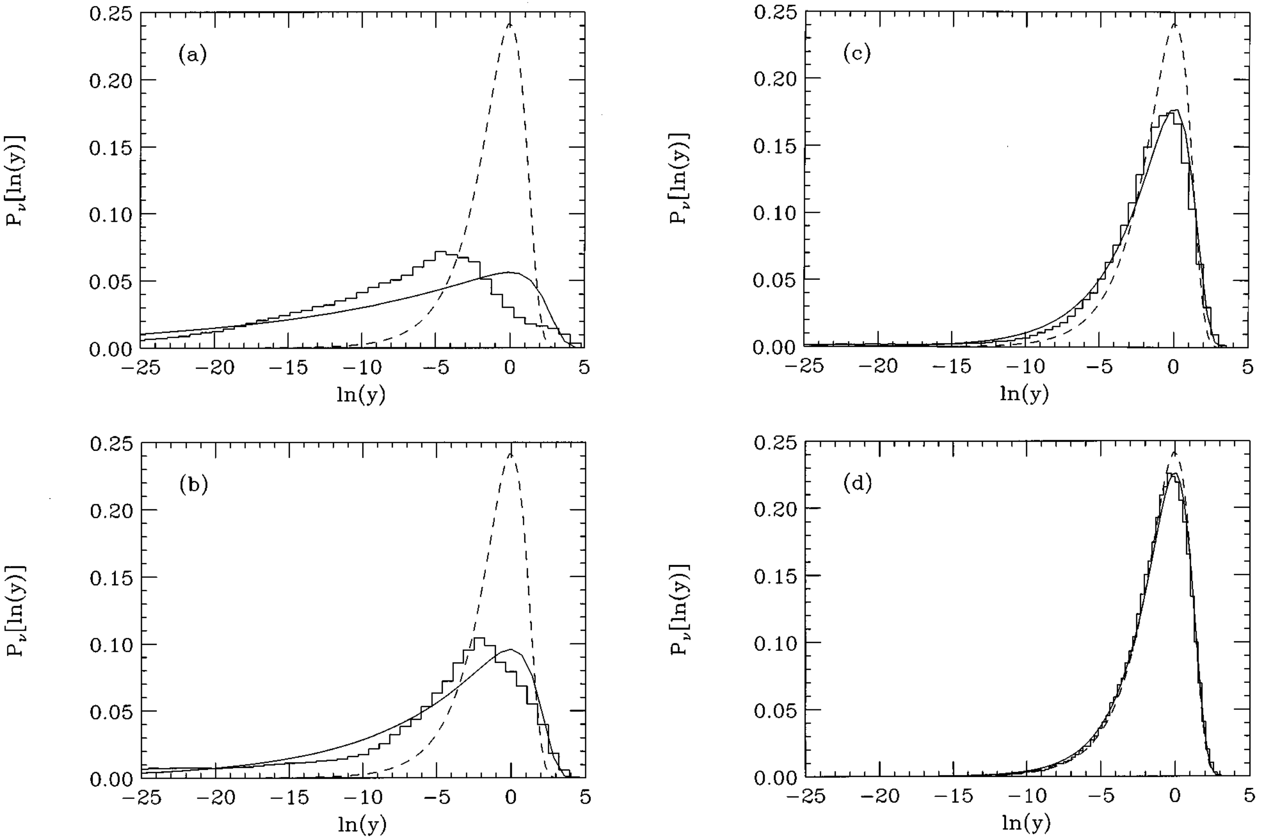

FIG. 7. (a)–(d) Distribution of amplitude overlaps of the QEF's with the natural basis states for the same $(\epsilon,\tilde{\omega}_c)$ values as in Figs. 2(a)–(d). Close to the COE limit (d), the amplitudes are nearly Gaussian or Porter-Thomas randomly distributed. Away from this limit the distributions are not well fitted by the $\chi^2$ distributions, with a significant difference seen close to the Poisson limit. This discrepancy is explained in the text. The values of $\nu$ from the fits are (a) 0.14, (b) 0.27, (c) 0.63, and (d) 0.9.

scaled so that $\langle y\rangle=1$.) We have tested this hypothesis for the overlap strengths for the same parameter values as for the quasienergy eigenvalue statistics. The results are shown in Fig. 7, plotted on a logarithmic scale. These results show the general trend of decreasing $\nu$ as we cross the phase boundary from regular to chaotic classical motion. However, we note that as we go from the COE to the Poisson limits, the fits to the $\chi^2$ get worse. Note especially the shift of the maxima away from zero. This discrepancy is connected to the fact that the results are strongly basis dependent when not in the universal COE limit.

### C. Semiclassical correspondences

We can now make a direct comparison between the classical and quantum results by employing a phase-space approach. To do this, we use the Husimi representation of the QEF. The Husimi distribution, interpreted as a probability density, is a coarse-grained version of the Wigner function that goes smoothly to the semiclassical limit [18]. In practice, the most often used technique of coarse graining is to take the overlap of the QEF with coherent oscillator states. For the radial coordinate the coherent state is

$$\Psi^G_{r_0,p_0}(r)=\left(\frac{\sigma}{\pi\tilde{\hbar}}\right)^{1/4}\exp\left\{-\frac{\sigma}{2\tilde{\hbar}}(r-r_0)^2+i\frac{p_0}{\tilde{\hbar}}\left(r-\frac{r_0}{2}\right)\right\}, \tag{32}$$

which is a minimum-uncertainty Gaussian wave packet centered at $(r_0,p_0)$, with root mean-square deviations given by $\Delta\rho=\sqrt{\tilde{\hbar}/2\sigma}$, $\Delta p=\sqrt{\tilde{\hbar}\sigma/2}$, and $\sigma$ is the "squeezing" parameter. This parameter is adjusted when making comparisons to the classical phase-space plots. The Husimi distribution of a single QEF $\phi_\varepsilon(r)$ is then defined by

$$\mathcal{F}_{\phi_\varepsilon}(r_0,p_0)=\left|\int_0^1\Psi^G_{r_0,p_0}(r)\phi_\varepsilon(r)dr\right|^2. \tag{33}$$

The Husimi distribution is obtained by scanning through the values of $(r_0,p_0)$ in the region of interest in phase space and the result is compared with the classical surface of section. We begin the comparison by noting the symmetry about the line $p=-\eta r$ in the Husimi contour plots in Fig. 8. As mentioned earlier, this feature carries over from the classical results. We in fact used to effectively halve the numerical effort.

All calculations reported here were carried out for relative cyclotron frequency $\tilde{\omega}_c=2\sqrt{2}$, angular momentum quantum number $l=5$, relative ac to dc field strength $\epsilon=1$, and scaled $\tilde{\hbar}=0.008$. In this case, all terms in the Hamiltonian are comparable in magnitude, which means that we are in a nonperturbative regime. Furthermore, we can clearly see both from the phase diagram and the surface of section that this places the system on the order-chaos border, where the dynamics is

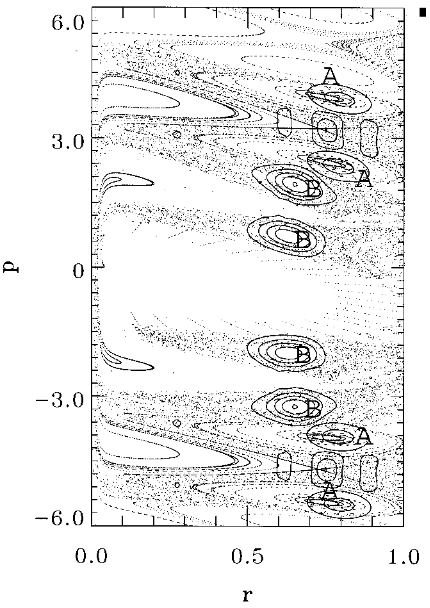

FIG. 8. Contour plots of the Husimi distribution of three QEF's. The Husimi distributions labeled $A$ correspond to the period-4 solution, while the one labeled $B$ is another example of an enhanced probability distribution over an elliptic fixed point of period 4. Finally, we also see a Husimi distribution of a QEF that corresponds to the period-6 hyperbolic orbit marked by its stable and unstable manifolds, a ''scarred'' eigenfunction. (The rectangle at the top-right corner indicates the uncertainties $\Delta X, \Delta P$.)

quite ''mixed.'' A few calculations were done for different values of the parameters, but no new qualitative features emerged. In choosing the value of $\tilde{\hbar}$, we were guided by the following considerations. The value of $\tilde{\hbar}$ has to be small enough so that the system is well into the semiclassical regime, yet large enough so that the dimension of the truncated Hilbert space $N$ (which grows as the inverse square of $\tilde{\hbar}$) is large enough to preserve unitarity. Moreover, $N$ has to be such that the largest eigenenergy of $H_{\text{dc}}$ has to be larger than the maximum energy of the classical particle in the region of interest in phase space. All the interesting features seen in this model are manifested in this regime. Finally, the classical conserved angular momentum $J$ was kept identical to the quantum value $l\tilde{\hbar}$.

The classical analysis was carried out for different values of the angular momentum $J$ [19]. First, we iterated a single (arbitrarily chosen) initial condition several thousand times, which typically leads to the chaotic background as shown in the figures. Embedded in this background are Kol'mogorov-Arnol'd-Moser (KAM) tori centered around elliptic fixed points, defined by choosing appropriate initial conditions. In Fig. 8 we show several such tori and in particular a fixed point of period 4 that was determined earlier analytically. Also shown in each of the figures is a hyperbolic fixed point of order 6, marked by its stable and unstable manifolds. The fixed points were determined by using a modified Powell method of determining zeros of coupled nonlinear sets of equations [20]. This method, like all multidimensional root-finding techniques, requires a good initial guess to converge to the fixed point, but once given it determines the root and the monodromy matrix equation (i.e., the Jacobian or the determinant of the linearized version of the map) reliably and accurately. The fixed points are elliptic, parabolic or hyperbolic if the discriminant obtained from the eigenvalues [i.e., $(\text{trace})^2-4(\text{determinant})$] is negative, zero, or positive, respectively. In all cases, it was verified, within numerical error, that the map was area preserving, i.e., the determinant was equal to one. The unstable manifold was obtained by iterating the map along the direction given by the eigenvector corresponding to the eigenvalue larger than one. The *stable* manifold is given by the time-reversed version of the unstable one.

A comparison of the Husimi distributions $\mathcal{F}_{\phi\varepsilon}(r_0,p_0)$ with the classical phase-space plots shows some striking similarities. There are, for many QEF's, many structures that unmistakably correspond to elliptic, parabolic, and hyperbolic periodic orbits, as seen in Fig. 8. For example, the Husimi representation of one of the QEF's sits on top of the analytic period-2 fixed point marked $F$. Also seen in the figure are Husimi distributions that peak *exactly* on top of the unstable hyperbolic period-6 fixed point, referred to in the literature as ''scars'' [21]. This correspondence is so robust, in fact, that often when a good guess to the *classical* hyperbolic fixed points is unavailable, the Husimi distributions are used as a guide to the location of the fixed point (being unstable, hyperbolic fixed points cannot be located without a very good initial guess). These enhanced probability densities are conjectured to play as important a role in quantum mechanics as the hyperbolic orbits play in classical chaos. Finally, a rare but persistent occurrence in all the cases considered is that of a single Husimi distribution peaked simultaneously over *both* elliptic and hyperbolic fixed points, reflecting a purely quantum-mechanical tunneling across the KAM tori. Here we have only shown representative results of the correspondence between Husimi distributions and classical solutions.

## V. EXPERIMENTAL FEASIBILITY

Before concluding, we present some experimental scenarios where the predicted effects may be observable. A ''typical'' GaAs-Al$_x$Ga$_{1-x}$As semiconductor quantum dot [22,23] has a radius $R_0$ between 0.1 and 10 $\mu$m, a sheet density $n \sim 10^{11}$ cm$^{-2}$, and a mobility $\mu \sim 2.65\times10^5$ cm$^2$/V s. The typical level spacing $\Delta\epsilon \sim 0.05$ meV or $\sim 500$ mK. The operating temperatures is generally of the order of 0.1 K, so $kT \sim 0.01$ meV is smaller than $\Delta\epsilon$ and thus the discrete spectrum can be accessed. A typical elastic mean free path $l_\phi \sim 10$ $\mu$m and the phase coherence length varies between 15 and 50 $\mu$m. The power injected is typically less than 1 nW, which avoids the problem of electron heating.

Given these parameters, we can estimate in physical units the field strengths and frequencies required to observe the effects predicted by our model. Let us first calculate these assuming a dot radius $R_0 \sim 1$ $\mu$m. The fundamental kick frequency $\omega_0$ in our problem can be deduced from Eq. (4b) as $\omega_0 = \hbar/(m^* R_0^2 \tilde{\hbar}) \simeq [1/\tilde{\hbar}]\, 2\times10^9$ s$^{-1}$. From this we can deduce the required dc and ac magnetic field magnitudes

$$B_{\text{dc}} = \frac{\omega_0 m^* c}{e}\tilde{\omega}_c \simeq 20\frac{\tilde{\omega}_c}{\tilde{\hbar}}\text{G}, \tag{34}$$

$$B_{ac}=\epsilon B_{\mathrm{dc}}\simeq 20\frac{\epsilon\widetilde{\omega}_c}{\widetilde{\hbar}}\ \mathrm{G}. \tag{35}$$

Finally, the Larmor frequency associated with the ac field is given by $\omega_{\mathrm{ac}}=\epsilon\widetilde{\omega}_c\simeq\epsilon\widetilde{\omega}_c/(\widetilde{\hbar})2\times10^7\mathrm{s}^{-1}$. The dot radius $R_0$ in Ref. [23] is about 5 $\mu$m. For this radius, the frequency and dc magnetic field magnitudes are $\omega_0\simeq 8\times10^7\ \mathrm{s}^{-1}\widetilde{\hbar}^{-1}$ and $B_{\mathrm{dc}}\simeq 0.8\widetilde{\omega}_c\ \widetilde{\hbar}^{-1}$Gauss.

With these values, we can see what physical parameters correspond to the integrable and chaotic regimes. We fix $\widetilde{\hbar}=0.1$ and choose as representative parameters $(\epsilon,\widetilde{\omega}_c)^{(\mathrm{reg})}=(0.1,0.1)$ where the motion is regular and the parameters $(\epsilon,\widetilde{\omega}_c)^{(\mathrm{chaos})}=(2.0,2.0)$ where the motion is chaotic. Then, for $R_0\sim1$ $\mu$m, the frequency and ac fields corresponding to the regular regime are

$$\omega_0^{(\mathrm{reg})}\simeq 20\ \mathrm{GHz},\quad B_{\mathrm{ac}}^{(\mathrm{reg})}\simeq 20\ \mathrm{G}, \tag{36}$$

while those corresponding to the chaotic regime are

$$\omega_0^{(\mathrm{chaos})}\simeq 20\ \mathrm{GHz},\quad B_{\mathrm{ac}}^{(\mathrm{chaos})}\simeq 800\ \mathrm{G}. \tag{37}$$

For the case $R_0\sim5$ $\mu$m, the frequencies and fields are, for the regular regime,

$$\omega_0^{(\mathrm{reg})}\simeq 800\ \mathrm{MHz},\quad B_{\mathrm{ac}}^{(\mathrm{reg})}\simeq 0.08\ \mathrm{G} \tag{38}$$

and, for the chaotic regime,

$$\omega_0^{(\mathrm{chaos})}\simeq 800\ \mathrm{MHz},\quad B_{\mathrm{ac}}^{(\mathrm{chaos})}\simeq 32\ \mathrm{G}. \tag{39}$$

With the appropriate techniques of measurement, for example, by using an array of $\sim10^5$ *isolated* quantum dots to increase the magnitude of the signal and using a highly sensitive electromagnetic superconducting microresonator to measure the response, as was done by Reulet *et al.* in Ref. [24] to measure the dynamic conductance of mesoscopic rings threaded by Aharonov-Bohm fluxes, we believe that an experimental realization of this system is feasible.

## VI. CONCLUSION

We have shown that the model of an electron in a rigid quantum dot structure subject to constant and periodically kicked magnetic fields shows a transition to chaos, depending on the relationship between the strengths of the fields and the cyclotron frequency of the steady field. This relationship is characterized by a phase diagram in parameter space, shown in Fig. 1. The nature of various periodic orbits was investigated. The quantum signatures of this transition are evidenced in two measures. First, as the classical system goes from integrable to chaotic, the statistics of the quasienergy spectrum follow the route from Poisson-like to COE-like. Second, the contour plots of the Husimi distribution of the quasienergy eigenfunctions clearly exhibit the phenomenon of scarring over unstable periodic orbits. Finally, we have presented some experimental ranges of the parameters where the effects of chaos in the system may be observable. To sum up, all tests applied to the classical quantum correspondence are in full agreement with the established quantum manifestations of classical chaos. The many-electron problem is planned to be treated elsewhere [25].

## ACKNOWLEDGMENTS

We thank G. Chu for useful discussions. This work was supported by Office of Naval Research Grant No. ONR-N00014-92-1666 and by NSF Grant No. DMR-95-21845.

## APPENDIX

In this appendix we show that the classical particle and field equations of motion can be written exactly for a periodically kicked magnetic field. Starting from the Lorenz force equation

$$m^*\frac{d^2\mathbf{r}}{dt^2}=m^*\frac{d\mathbf{v}}{dt}=e\left\{\frac{\mathbf{v}}{c}\times\mathbf{B}(t)+\mathbf{E}(t)\right\}, \tag{A1a}$$

where

$$\mathbf{B}(t)=\left(B_{\mathrm{dc}}+B_{\mathrm{ac}}T_0\sum_{n=-\infty}^{\infty}\delta(t-nT_0)\right)\hat{\boldsymbol{e}}_z\equiv\{B_{\mathrm{dc}}+B_{\mathrm{ac}}\Delta(t)\}\hat{\boldsymbol{e}}_z \tag{A1b}$$

and

$$\mathbf{E}(t)=-\frac{1}{c}\frac{\partial}{\partial t}\mathbf{A}(t)=\frac{B_{\mathrm{ac}}}{2c}\dot{\Delta}(t)(\mathbf{r}\times\hat{\boldsymbol{e}}_z), \tag{A1c}$$

then, on substituting Eqs. (A1b) and (A1c) into Eq. (A1a) and using the definition of $\omega_c$, we get

$$\frac{d\mathbf{v}}{dt}=\omega_c(\mathbf{v}\times\hat{\boldsymbol{e}}_z)+\epsilon\omega_c(\mathbf{v}\times\hat{\boldsymbol{e}}_z)\Delta(t)+\frac{\epsilon\omega_c}{2}(\mathbf{r}\times\hat{\boldsymbol{e}}_z)\dot{\Delta}(t). \tag{A2}$$

Using the standard property of the $\delta$ function $\int f(x)\delta'(x-a)dx=-f'(a)$, the last term becomes $(\epsilon=B_{\mathrm{ac}}/B_{\mathrm{dc}})$

$$\frac{\epsilon\omega_c}{2}(\mathbf{v}\times\hat{\boldsymbol{e}}_z)\Delta(t). \tag{A3}$$

Thus the *exact* equations of motion can be written as

$$\frac{d\mathbf{v}}{dt}=\omega_c(\mathbf{v}\times\hat{\boldsymbol{e}}_z)\left\{1+\frac{\epsilon}{2}T_0\sum_{n=-\infty}^{\infty}\delta(t-nT_0)\right\}. \tag{A4}$$

Note that the only difference we have from including the induced **E** field is a factor of 1/2 in the kicked component of the **B** field.

The reason the same analysis cannot be done the same way in the quantum problem is that there it is the vector potential that is the relevant dynamical variable. Thus, if we use an $\mathbf{A}=\mathbf{A}_{\mathrm{dc}}+\mathbf{A}_{\mathrm{ac}}(t)$ with $\mathbf{A}_{\mathrm{ac}}(t)\simeq\Sigma_{n=-\infty}^{\infty}B_{\mathrm{ac}}(\rho)\delta(t-nT_0)$, we see that we have a mathematical ambiguity in the definition of $\mathbf{A}_{\mathrm{ac}}^2$. Nonetheless, one can carry out the nonrelativistic analysis with our model Hamiltonian that contains, we believe, the essential physics of the problem and yet is mathematically tractable.

[1] V. Fock, Z. Phys. **47**, 446 (1928); L. Landau, Z. Phys. **64**, 629 (1930).

[2] R. B. Dingle, Proc. R. London Ser. Soc. A **211**, 500 (1952); **212**, 47 (1952).

[3] M. Robnik, J. Phys. A **19**, 3619 (1986).

[4] *The Quantum Hall Effect*, 2nd ed., edited by R. Prange and S. Girvin (Springer-Verlag, New York, 1990).

[5] For a review, see A. J. Lichtenberg and A. M. Lieberman, *Regular and Chaotic Dynamics*, 2nd ed. (Springer-Verlag, New York, 1992).

[6] For a recent comprehensive overview, see *Quantum Chaos: Between Order and Disorder,* edited by G. Casati and B. Chirikov (Cambridge University Press, Cambridge, 1995).

[7] C. W. J. Beenakker and H. van Houten, in *Solid State Physics*, edited by H. Ehrenreich and D. Turnbull (Academic, New York, 1991), Vol. 44, p. 1.

[8] L. J. Slater, *Handbook of Mathematical Functions,* Natl. Bur. Stand. Appl. Math. Ser. No. 55, edited by Milton Abramowitz and Irene A. Stegun (U.S. GPO, Washington, DC, 1968), p. 503.

[9] G. Casati and L. Molinari, Prog. Theor. Phys. Suppl. **98**, 287 (1989).

[10] L. E. Reichl, *The Transition to Chaos in Conservative Classical Systems: Quantum Manifestations* (Springer-Verlag, New York, 1992).

[11] O. Bohigas, M.-J. Giannoni, and C. Schmit, Phys. Rev. Lett. **52**, 1 (1984).

[12] J. V. José and R. Cordery, Phys. Rev. Lett. **56**, 290 (1986).

[13] T. A. Brody, Lett. Nuovo Cimento **7**, 482 (1973).

[14] O. Bohigas and M.-J. Giannoni, in *Mathematical and Computational Methods in Nuclear Physics*, edited by J. S. Dehesa *et al.* (Springer-Verlag, Berlin, 1984).

[15] M. L. Mehta, *Random Matrices: An Enlarged and Revised Second Edition* (Academic, New York, 1991).

[16] M. V. Berry, Proc. R. Soc. London Ser. A **400**, 299 (1985).

[17] Y. Alhassid and R. D. Levine, Phys. Rev. Lett. **57**, 2879 (1986); K. Zyczkowski, J. Phys. A **23**, 4427 (1991).

[18] S.-J. Chang and K.-J. Shi, Phys. Rev. A **34**, 7 (1986).

[19] The classical analysis parallels a similar calculation for a different problem; see R. Badrinarayanan, J. V. José, and G. Chu, Physica D **83**, 1 (1995); see also, G. Chu and J. V. José, J. Stat. Phys. **68**, 153 (1992).

[20] W. H. Press *et al.*, *Numerical Recipes in Fortran*, 2nd ed. (Cambridge University Press, Cambridge, 1992), p. 406.

[21] R. V. Jensen, M. M. Sanders, and M. Saraceno, Phys. Rev. Lett. **63**, 2771 (1989).

[22] C. M. Marcus *et al.*, Phys. Rev. Lett. **69**, 506 (1992).

[23] L. P. Lévy, D. H. Reich, L. Pfeiffer, and K. West, Physica B **189**, 204 (1993).

[24] B. Reulet, M. Ramin, H. Bouchiat, and D. Mailly, Phys. Rev. Lett. **75**, 124 (1995).

[25] R. Badrinarayanan and J. V. José (unpublished.)